arXiv:hep-ph/9606268v1 7 Jun 1996

Higgs signals and hard photons via WW-fusion
in the Standard Model
at the Next Linear Collider

Stefano Moretti[1]

Dipartimento di Fisica Teorica, Università di Torino,
and I.N.F.N., Sezione di Torino,
Via Pietro Giuria 1, 10125 Torino, Italy.

Cavendish Laboratory, University of Cambridge,
Madingley Road, Cambridge, CB3 0HE, United Kingdom.

PACS numbers: 14.80.Bn, 14.70.Bh, 14.70.Fm, 29.17.+w.

Abstract

Within the framework of the Standard Model, integrated and differential distributions are given for Higgs production via the WW-fusion mechanism and decay via the channels $H \to b\bar{b}$ and $H \to WW \to$ jjjj, with and without photon radiation, at Next Linear Collider energies. Calculations are carried out at tree-level and rates of the leading processes $e^+e^- \to \bar{\nu}_e\nu_e H \to \bar{\nu}_e\nu_e b\bar{b}$ and $e^+e^- \to \bar{\nu}_e\nu_e H \to \bar{\nu}_e\nu_e WW \to \bar{\nu}_e\nu_e$jjjj are compared to those of the next-to-leading reactions $e^+e^- \to \bar{\nu}_e\nu_e H(\gamma) \to \bar{\nu}_e\nu_e b\bar{b}\gamma$ and $e^+e^- \to \bar{\nu}_e\nu_e H(\gamma) \to \bar{\nu}_e\nu_e WW(\gamma) \to \bar{\nu}_e\nu_e$jjjj$\gamma$, in the case of hard and detectable photons. Finally, a brief discussion concerning the case of $H \to ZZ \to$ jjjj(γ) decays is also given.

---

[1]E-mails: Moretti@to.infn.it; Moretti@hep.phy.cam.ac.uk.

1. Introduction

The motivations for building an e^+e^- linear collider operating in the energy range $\sqrt{s} = 300 - 1000$ GeV (NLC, Next Linear Collider) are indeed quite convincing [1, 2, 3, 4, 5]. For example, one of the major goals of such a machine will be to perform 'high precision' Higgs physics. That is, to measure the parameters (mass M_H, width Γ_H, spin $\mathcal{S}_H$, $\{\mathcal{J}^{PC}\}_H$ quantum numbers, etc.) and the relevant phenomenological rates (cross sections, branching ratios, etc.) of the Higgs boson H, to an accuracy that can not be achieved at hadron machines. The importance of this project is clear if one considers that the Higgs mechanism of spontaneous symmetry breaking is a sort of 'pedestal' that holds up the entire Standard Model ($\mathcal{SM}$).

If it exists, the H particle will be probably discovered at the Large Hadron Collider (LHC) [6], which is expected to start running early next century, well in advance of the future NLC. The CERN pp collider will however have great difficulties in measuring the fundamental quantities related to this particle, because of the huge background proceeding via strong interactions which will be present at the hadron machine. This is particularly true for a Higgs boson in the intermediate mass range (IMR), $M_H \lesssim 2M_W$, for which the detectability of the only two viable decay channels, $H \to \gamma\gamma$ and $H \to b\bar{b}$, strongly depends on the detector performances. For a Higgs in the heavy mass range (HMR), $M_H \gtrsim 2M_W$, things should be easier, as the four-lepton decay mode $H \to ZZ \to 4\ell$ is relatively clean and straightforward to detect.

At the NLC, the main $\mathcal{SM}$ Higgs production mechanisms are via the bremsstrahlung process $e^+e^- \to ZH$ [7] and via the WW- and ZZ-fusion reactions $e^+e^- \to \bar{\nu}_e\nu_e WW(e^+e^- ZZ) \to \bar{\nu}_e\nu_e(e^+e^-)H$ [8]. For a first stage NLC (with $\sqrt{s} \lesssim 500$ GeV) the rates of the bremsstrahlung mechanism are larger than those of the fusion channels, if $M_H \lesssim 2M_W$. At larger centre-of-mass (CM) energies ($\sqrt{s} \gtrsim 500$ GeV) WW-fusion starts dominating over the whole of the M_H spectrum. Furthermore, the rates of ZZ-fusion are generally one order of magnitude smaller than those of the WW-channel. Concerning possible Higgs signatures, all the principal decay modes of this particle can be detected and studied at the NLC, for all values of M_H, provided that enough statistics can be accumulated [9]. In particular, the main sources of Higgs events will be the channels $H \to b\bar{b}$ (IMR) and $H \to WW \to 4$jet (HMR) [10].

There are a few important aspects, in the way a NLC running around the TeV energy scale will operate, that should be carefully considered in order to exploit in full its potential and that are absent in lower energy e^+e^- machines. These are related to the influence on the cross sections of electromagnetic (EM) interactions which can take place before the actual beam collision, such as *bremsstrahlung* and *beamsstrahlung* effects [11][2]. Whereas effects due to synchrotron radiation emitted by one of the colliding bunches in the field of the other one (i.e.,

---

[2]Effects due to the energy spread of the beams before annihilation (intrinsic to any collider) should also be considered.

beamsstrahlung) necessarily need, in order to be quantified, the knowledge of the technical details of the collider design and can be realistically estimated only through Monte Carlo simulations, those due to the emission and exchange of photons from and between the actual pair of electron and positron which collide (i.e., bremsstrahlung or Initial State Radiation, ISR), can be treated in a fairly general way. In many cases, one can compute the exact EM corrections to the e^+e^- annihilation subprocess and express these via the so-called 'electron structure functions'. Such corrections embody both real and virtual photon radiation and they are known to date up to the order $\mathcal{O}(\alpha_{\text{em}}^2)$ [12]. It has also been shown that, for 'narrow beam' designs, beamsstrahlung affects the cross section much less than the ISR [11], such that in phenomenological analyses one can consistently confine oneself to dealing with bremsstrahlung radiation only. In general, the principle effect of the ISR is to lower the effective CM energy available in the main process, thus ultimately reducing(enhancing) total cross sections which increase(decrease) at larger CM energies. Furthermore, ISR also leads to a smearing of the differential distributions [13]. However, the 'electron structure functions' approach is not always applicable, such as in the context of WW-fusion processes in e^+e^- annihilations.

It is the purpose of this paper to study the properties and the effect on the integrated rates as well as on the differential distributions of interest to Higgs searches of *hard photon* emission, which can take place in the $\mathcal{SM}$ Higgs production and decay processes

$$e^+e^- \to \bar{\nu}_e\nu_e H(\gamma) \to \bar{\nu}_e\nu_e b\bar{b}\gamma, \tag{1}$$

$$e^+e^- \to \bar{\nu}_e\nu_e H(\gamma) \to \bar{\nu}_e\nu_e WW(\gamma) \to \bar{\nu}_e\nu_e\text{jjjj}\gamma, \tag{2}$$

(that is, via the WW-fusion mechanism), at NLC energies and for several values of the Higgs mass, and where the photon can be emitted from the initial, virtual and final states. In our opinion, the importance of this study is motivated by the fact that, contrary to lower energy e^+e^- colliders (such as LEP1, SLC and in part also LEP2), which 'sit' on gauge boson resonances and so the width of the unstable particles imposes a natural cut-off on events with hard photons produced by the initial state, at the NLC such a suppression does not act any longer. In addition, as the beam energy is much larger, the probability that the incoming electrons and positrons can radiate hard photons increases greatly. From this, it follows that in practise a sample of pure $e^+e^- \to \bar{\nu}_e\nu_e b\bar{b}$ and $e^+e^- \to \bar{\nu}_e\nu_e\text{jjjj}$ events, without γ-radiation, does not exist and one inevitably has to deal with EM emission. Moreover, in the experimental samples of data, events in which the photon is emitted during the production process $e^+e^- \to \bar{\nu}_e\nu_e H\gamma$ are not distinguishable from those in which the radiation comes from the Higgs decay stages $H \to b\bar{b}\gamma$ and $H \to WW(\gamma) \to \text{jjjj}\gamma$, such that in phenomenological simulations one is forced to consider both the cases at the same time. In particular, we stress that it is principally the second kind of radiation which could spoil the shape of the Higgs resonances.

The plan of the paper is as follows. In Sec. 2 we devote some space to illustrate the computational techniques that we have used as well as the numerical values adopted. Sec. 3 presents our results, and in Sec. 4 we give a summary and report the main conclusions to be drawn from this study.

2. Calculation

The Feynman diagrams corresponding to processes (1)–(2) are given in Figs. 1 and 2, respectively. To compute them we have adopted numerical techniques which use the helicity amplitude formulae of Ref. [14] and the subroutines contained in the package HELAS [15]. For process (1) we have also resorted to the program MadGraph [16] for the generation of the `FORTRAN` code of the Matrix Element (ME). The routine `VEGAS` [17] has been used as multi-dimensional integrator. To achieve high accuracy in the evaluation of the cross sections in presence of Higgs peaks in different regions of the phase space, we have used the method of splitting the Feynman amplitudes squared into non-gauge invariant terms, each of which with a different peak structure. These have been then integrated separately by using an appropriate choice of the phase space variables, according to the resonant behaviour of the graphs involved. A sum over the various terms of the MEs gives in the end gauge-invariant results. Such a procedure has been already described elsewhere (for example, in Ref. [18]), such that we do not enter here into details.

The computation of the graphs in Figs. 1–2 is rather straightforward, though the numerical integrations over the phase space can in some instances be rather complicated, as they can involve up to 16 dimensions[3]. Thus, in order to perform our calculations in a reasonable amount of CPU time we have always constrained the W-bosons to be on-shell in process (2)[4]. In this way, we are able to reduce by two the number of the variables we integrated over. As we will be eventually interested in studying the invariant mass distributions of the decay products of the Higgs boson, we expect such a procedure to have a little impact on our final results. However, a direct consequence of this simplification is that we are not able to study Higgs decays into four jets below and near the $2M_W$ threshold. Nonetheless, since the phenomenology of the off-shell Higgs decay $H \to W^*W^*$ is well known, predictions in the range $M_H \lesssim 2M_W$ can be easily extrapolated from our rates. For consistency, we have constrained the W-bosons to be on-shell

---

[3]Corresponding to a final state of 7 particles, in case of process (2).

[4]Both in the case of process (1) and in the lowest order reaction

$$e^+e^- \to \bar{\nu}_e \nu_e H \to \bar{\nu}_e \nu_e b\bar{b}, \tag{3}$$

no simplification in any respect has been adopted.

also in the case of the leading process

$$e^+e^- \rightarrow \bar{\nu}_e\nu_e H \rightarrow \bar{\nu}_e\nu_e WW \rightarrow \bar{\nu}_e\nu_e\text{jjjj}. \tag{4}$$

Furthermore, the interferences between the various peaks in processes (1)–(2) are in general very small compared to the squared terms of the resonances and do not bring any distinctive structure into the differential distributions. In fact, such contributions always mix up graphs with different resonant structures[5], such that the phase space regions in which one or more amplitudes are large are different for different graphs. Therefore, as a further simplification, such interferences have been systematically neglected in the presentation of our results.

The following numerical values of the parameters have been adopted: $M_Z = 91.175$ GeV, $\Gamma_Z = 2.5$ GeV, $M_W = 80.23$ GeV, and for the Weinberg angle we have used its leptonic effective value $\sin^2_{\text{eff}}(\theta_W) = 0.2320$. For the fermions: $m_e = m_{\nu_e}=0$, $m_b = 4.25$ GeV, whereas all light quarks u, d, s and c have been considered massless. Jets have been identified with the partons from which they originate. The EM coupling constant α_{em} has been set equal to 1/128. For the Higgs width Γ_H we have adopted the tree-level expression corrected for the running of the quark masses in the vertices $Hq\bar{q}$ (these have been evaluated at the scale $\mu = M_H$ [19]). Therefore, in order to be consistent, we have used a running b-mass in the $H \rightarrow b\bar{b}$ vertex of the production processes (1) and (3). As representative values of the CM energy of the NLC we have adopted 300, 500 and 1000 GeV, and the Higgs mass has been chosen in the range 60 GeV $\lesssim M_H \lesssim$ 450 GeV.

3. Results

Photon radiation can be emitted in processes (1)–(2) both during the production mechanism $e^+e^- \rightarrow \bar{\nu}_e\nu_e H\gamma$ and during the decays $H \rightarrow b\bar{b}\gamma$ and $H \rightarrow \bar{\nu}_e\nu_e\text{jjjj}\gamma$. The emission is gauge-invariant in both these two stages and we will refer to it as 'production radiation' and 'decay radiation', respectively. The ISR as previously defined would correspond here to the photons emitted by the incoming electron and positron lines. The diagrams describing such bremsstrahlung (i.e., graphs 1–2 in both Fig. 1–2) do not satisfy gauge-invariance if taken on their own. To recover the latter it is needed to add the graphs in which the photon is emitted by the W-lines (i.e., graphs 5–6 in both Fig. 1–2). Therefore, a separation of the ISR diagrams from the rest does not make sense here. The issue of defining the ISR in a gauge-invariant way in presence of charged current (CC) interactions is indeed a well known problem, for example in case of $e^+e^- \rightarrow W^+W^- \rightarrow 4$ fermions production at LEP2. In the sense that, in

---

[5]We have integrated them by using a flat phase space, which does not map any of the possible peaks of the interfering graphs.

presence of electric charge flow between the initial and the subsequent stages of e^+e^--initiated processes, the definition of the ISR is not unique. Such a difficulty has been probably overcome in the case of neutrino exchange, by means of the so-called *current splitting technique* (for details, see Ref. [20]). In that case, complete ISR separates into a universal, factorising, process independent-contribution (that is, the electron structure functions of Ref. [12]) and a non-universal, non-factorising, process-dependent part (that is, the complex analytical expressions as given in Ref. [21]). However, this approach is not realistically possible in the present context. In fact, the formulae of Refs. [12, 21] are valid only in case of *annihilation*- and *conversion*-type Feynman diagrams, that is, when the incoming e^+- and e^--lines are connected to each other via a s- or t, u-channel, respectively. In contrast, we are concerned here with electron/positron lines that are disconnected from each other and that end up as the (anti)neutrino ones of the final states, by means of multiple space-like CC-interactions.

The most correct approach would certainly be to compute the complete $\mathcal{O}(\alpha_{\mathrm{em}})$ (and beyond) corrections, including the loop diagrams. That is however beyond the intentions of this study. What we will do here is to show results for the leading order (LO) processes (3)–(4) and the next-to-leading order (NLO) ones (1)–(2) separately, the latter with real photons having $p_T^\gamma > 1$ GeV (hard and detectable EM radiation), in terms of both integrated and differential rates. We also impose an additional cut on the photon, by asking that the latter be isolated from the jets arising in the final states of processes (1)–(2), from the b- and the light quarks: for example, by imposing $\cos\theta_{b\gamma,\ j\gamma} < 0.95$ (corresponding to a cone with an angular size of ≈ 18 degrees). This is done because it would generally be impossible to tag photons too close to the original parton, as the latter gives rise to a jet with a finite angular size, such that if the photon fails within the corresponding cone it will not be distinguished from the other parts of the jets. In this case, its energy is counted as part of that of the hadronic system associated with the parton and the $M_{b\bar{b}}$ and M_{jjjj} invariant masses are not experimentally measurable in events of the type (1)–(2). For configurations in which the photon is highly collinear (i.e., $\cos\theta_{b\gamma,\ j\gamma} \geq 0.95$), such events would rather be recognised as leading $2 \to 4$ and $2 \to 6$ topologies.

In order to be consistent with the sketched approach, we will refrain from summing up lowest and next-to-lowest rates through the orders $\mathcal{O}(\alpha_{\mathrm{em}}^5)$ and $\mathcal{O}(\alpha_{\mathrm{em}}^7)$, as such a summation would need to include also the contributions due to virtual photons. In practise then, the aim of our study is, on the one hand, to estimate the size of the rates produced by events with hard photons and, on the other hand, to compare their kinematic properties to those of the non-radiative processes. This is done in order to establish whether the shape of the differential spectra of interest to Higgs searches can be significantly modified at higher order by the presence of hard photons, such that when proceeding to experimental analyses one might expect a smearing of the relevant resonant distributions. In particular, we remind the reader that the contributions that

we have not computed (the loop diagrams) or removed by the cuts (the infrared photon regions) would show the same kinematics as the lowest order processes, such that they would modify the overall normalisation of the differential distributions but not the shape. In particular, concerning the 'decay radiation', it is well known that the Kinoshita-Lee-Nauenberg theorem [22] prescribes that all the logarithmic contributions of the form $(\alpha_{\rm em}/\pi)^n \ln^n(s/m_{b,\,j}^2)$, which appear to the order $\mathcal{O}(\alpha_{\rm em})^n$ according to the Sudakov theorem [23] and which are due to 'collinear' emission of photons from the final state, must not appear in the expression of the inclusive cross section. They are in fact canceled by the *negative* contributions due to virtual final state photons. Therefore, the hard photon effects that we will discuss in the following could well be larger in the complete $\mathcal{O}(\alpha_{\rm em})$ result. In the very end, in order to compare theory and experiment, the latter are certainly needed. However, our preliminary results will enable us to assess whether, at higher order, complications should be expected in individuating the position of the peaks and/or in establishing their line-shape, or whether the effect of $\mathcal{O}(\alpha_{\rm em})$ corrections is mainly matter of overall normalisation of the leading order distributions.

In our analysis, we will present spectra in $M_{b\bar{b}}$, $M_{b\bar{b}\gamma}$, $M_{\rm jjjj}$, $M_{\rm jjjj\gamma}$ (that is, in the invariant masses of the decay products $b\bar{b}(\gamma)$ and jjjj(γ) of the Higgs scalar), together with those in E_γ (the energy of the photon) and in $p_T^{\rm miss}$ (the missing transverse momentum of the undetected neutrino pair). The importance of the distributions in invariant mass is clear if one considers that the presence of 'decay radiation' could spoil in the end the form of the Breit-Wigner peaks in $M_{b\bar{b}}$ and $M_{\rm jjjj}$ that one obtains from the LO contributions (3)–(4), via diagrams 3–4 in Fig. 1 and 3–4 & 7–10 in Fig. 2. On the other hand, these diagrams contribute to produce Higgs resonances in the $M_{b\bar{b}\gamma}$ and $M_{\rm jjjj\gamma}$ spectra. In contrast, the EM emission that takes place via the 'production radiation' should not significantly spoil the form of the peaks[6] and should instead contribute to enhance the number of resonant events. The distributions in E_γ and $p_T^{\rm miss}$ could in principle be useful in order to separate in events of the type (1)–(2) contributions due to 'production radiation' from those due to 'decay radiation', provided significant differences exist between the corresponding differential spectra. In particular, these can be exploited in order to enrich the experimental sample of events with photons not emitted during the Higgs decays. Also, their knowledge could eventually be useful in disentangling Higgs signal from background processes (both irreducible and reducible ones).

Finally, the cut on the transverse momentum of the photon has actually also been applied to all other particles in the final states of reactions (1)–(4), apart from the neutrinos. Such a constraint should generally meet the requirements due to the finite coverage in energy and polar angle of the NLC detectors.

---

[6] Its effect being mainly confined to lower the invariant mass of the WW-annihilation into the Higgs boson.

3.1. The Higgs process $e^+e^- \to \bar{\nu}_e\nu_e b\bar{b}\gamma$

We first consider the $b\bar{b}$ Higgs decay channel. The cross sections for processes (1) and (3) are given in Fig. 3, for the mentioned choice of CM energies. They are presented as a function of the Higgs mass M_H. For illustrative purposes we have considered the mass range 60 GeV $\lesssim M_H \lesssim 350$ GeV, however the largest rates occur for $M_H \lesssim 140$ GeV (intermediate mass range), where the $H \to b\bar{b}$ decay has the largest branching ratio (BR). For $M_H \gtrsim 140$ GeV the off-shell channel $H \to W^*W^*$ starts dominating the $\mathcal{SM}$ Higgs decay phenomenology. This is reflected in the steep decrease of the cross sections, both at leading and next-to-leading order, slightly before the real $2M_W$ threshold.

The main feature of Fig. 3 is certainly the relatively large value of the rates for the radiative process (1) compared to those of the non-radiative reaction (3). In fact, the former is at least 10% of the latter over all the interesting range of M_H, at all values of $\sqrt{s}$. It increases with the CM energy and it is largely independent of the Higgs mass. In particular, if one assumes an integrated luminosity of $\int \mathcal{L}dt = 10$ fb^{-1}, more than 300 events with hard photons could be produced per year, at a NLC with $\sqrt{s} = 1000$ GeV and for $M_H \approx 60$ GeV. Such a number gets smaller with decreasing CM energy and increasing Higgs mass.

The kinematic properties of events of the type (1) and (3) are illustrated in Figs. 5a–c, for $\sqrt{s} = 300, 500$ and 1000 GeV, respectively. The selection of Higgs masses we have chosen here is $M_H = 60, 100$ and 140 GeV. For these values, the Higgs width is rather small, $\Gamma_H \lesssim 8$ MeV, such that hard photon emission in the decay process $H \to b\bar{b}\gamma$ (diagrams 3–4 in Fig. 1) is heavily suppressed. In fact, the contribution due to the two mentioned diagrams to the total cross section in $e^+e^- \to \bar{\nu}_e\nu_e H(\gamma) \to \bar{\nu}_e\nu_e b\bar{b}\gamma$ events is rather small (by more than one order of magnitude, for all $\sqrt{s}$ and M_H combinations) compared to the contribution due to graphs 1–2 & 5–6 in Fig. 1, that is when the photon is emitted by the electron/positron and gauge boson lines. This is clearly reflected in the NLO $M_{b\bar{b}}$ invariant mass distribution (upper left in Figs. 5a–c). In fact, the smearing towards low masses of the Higgs peaks due to the photon emission in the radiative $H \to b\bar{b}\gamma$ decay is essentially irrelevant for realistic phenomenological analyses: at the level of $\mathcal{O}(10^{-2})$ or even less[7].

The suppression of the 'decay radiation' is also visible in the invariant mass of the $b\bar{b}\gamma$ system (upper right plots in Figs. 5a–c). In the sense that the corresponding spectra show a step (rather than a peak) at $M_{b\bar{b}\gamma} \approx M_H$, with a long and quantitatively relevant tail for $M_{b\bar{b}\gamma} > M_H$, due to the photons from the 'production radiation'. In practise, the latter largely 'overwhelm' those originating in the 'decay radiation', which would produce a Breit-Wigner peak.

The distribution in energy of the radiated photon is displayed in the bottom left plots of

---

[7]Note the logarithmic scale in all the figures.

the same figures. It is qualitatively the same regardless of the actual value of the Higgs mass. In particular, very hard photons are suppressed at smaller (see Fig. 5a) and enhanced at larger (see Fig. 5c) CM energies, while the dependence of the spectrum at 500 GeV (see Fig. 5b) is roughly exponential. An additional suppression comes with the increase of the Higgs mass, at fixed $\sqrt{s}$, especially if $\sqrt{s} \leq 500$ GeV, whereas for $\sqrt{s} = 1000$ GeV such an effect is quite small. Furthermore, as one expects, the 'decay radiation' photons are always softer than the 'production radiation' ones.

The distribution in missing transverse momentum is rather similar for both processes (1) and (3) (bottom right of the mentioned figures) and for the two radiative components at NLO (for this reason the latter are not shown separately here). In general, the p_T^{miss} spectrum is only slightly harder for the non-radiative process. The maximum of the distribution is more pronounced as the CM energy increases and does not depend on the values of M_H.

3.2. The Higgs process $e^+e^- \to \bar{\nu}_e\nu_e\text{jjjj}\gamma$

Integrated cross sections at the CM energies $\sqrt{s} = 300, 500$ and 1000 GeV for processes (2) and (4) are shown in Fig. 4, as a function of the Higgs mass in the heavy mass range[8]. Whereas at lower values of $\sqrt{s}$ (upper plot) the production of a Higgs scalar with $M_H \gtrsim 180$ GeV is heavily suppressed, at larger CM energies (central and lower plots) rates are high enough to produce Higgs bosons up to masses of 450 GeV or so. In particular, at $\sqrt{s} = 1000$ GeV, cross sections for both processes (2) and (4) diminish by only a factor of 8 if M_H increases from 180 to 450 GeV. In contrast, at $\sqrt{s} = 300$ GeV, there is a steep decrease of the rates as M_H approaches $\sqrt{s}$. Curiously, in this case, the shape of the curves is rather similar to those of processes (1) and (3) (Fig. 3 upper plot). However, there the effect was due to the Higgs branching ratio, whereas here it occurs because of a phase space suppression on the production mechanism. Again, the most remarkable feature of Fig. 4 is a large rate for the radiative reaction (2), compared to the lowest order one (4). This is generally true for all relevant combinations of masses and energies. The ratio between the rates of the two processes is less than a factor of 10, and up to 100 radiative events per year can be expected (lower plot for the minimum Higgs mass).

Figs. 6a–c show the kinematic properties of the particles in the finale state of reactions (2) and (4). Since in the heavy mass range the Higgs width is quite large (it varies from ≈ 0.6 GeV at 180 GeV to ≈ 40 GeV at 460 GeV !), hard photon radiation in the Higgs decay is no longer suppressed (unlike the case of $H \to b\bar{b}\gamma$ radiative decays), especially at large Higgs masses. Moreover, in process (2), there are six graphs which contribute to produce a peak in the

---

[8]We consider values of M_H (greater than 180 GeV) far above the real WW threshold at $2M_W \approx 160$ GeV, in order to avoid complications due to having adopted here a narrow width approximation for the W boson, when the real value of Γ_W is instead around 2 GeV.

invariant mass of the jjjjγ system (i.e., number 3–4 & 7–10 in Fig. 2), since in the decay process $H \to WW \to (\gamma)$jjjjγ photon emission can take place off two boson and four fermion lines. These two aspects (i.e., large Higgs width and 'multiple' emission) act in such a way that in the end the amplitude squared corresponding to the contribution of the six mentioned diagrams ('decay radiation') is comparable to that of the others graphs ('production radiation'), over all the M_H spectrum and for all values of $\sqrt{s}$ considered here. This can be clearly appreciated by looking at the $M_{\mathrm{jjjj}\gamma}$ spectra (Figs. 6a–c, upper right). All the distributions in invariant mass of the jjjjγ system show a clear peak around the selected values of M_H (upper right plots in Figs. 6a–c). When the Higgs boson is lighter, such that its width is relatively narrow (for 180 GeV in the plots), many hard photons still come from the 'production radiation', giving the long tail especially visible in the continuous lines, similarly to process (1). However, contrary to the case of $H \to b\bar{b}\gamma$ resonant decays, here the peaks at $M_{\mathrm{jjjj}\gamma} \approx M_H$ remain visible. When instead the Higgs width is larger (for $M_H \gtrsim 220$ GeV in the plots), a large part of the photons come from the 'decay radiation', such that they contribute to build up a rather clear resonant dependence and the tail at $M_{\mathrm{jjjj}\gamma} > M_H$ starts disappearing (dotted and dashed lines). It is worth noticing that a phase space effect also contributes to enhance the above suppression at large values of $M_{\mathrm{jjjj}\gamma}$, such that in the end, in some instances (for example, at $\sqrt{s} = 300$ GeV and $M_H \gtrsim 220$ GeV, Fig. 6a), the NLO $M_{\mathrm{jjjj}\gamma}$ and M_{jjjj} distributions look pretty similar.

When considering the case of the distributions in M_{jjjj} at NLO, effects due to phase space enhancement/suppression play a more determinant rôle. In the sense that, when the portion of phase space available is restricted (that is at $\sqrt{s} = 300$ GeV, Fig. 6a upper left, the shaded curves) the main effect due to the hard photons is the appearance of a tail at $M_{\mathrm{jjjj}} < M_H$ (see especially the cases $M_H = 220$ and 260 GeV). This is a consequence of a superposition of a rather symmetrical resonance (due to the 'production radiation' diagrams, whose shape looks similar to the one at LO, appropriately rescaled) and of a spectrum (due to the 'decay radiation' diagrams) that is strongly shifted towards low invariant masses[9]. As $\sqrt{s}$ increases the low mass tail effect due to diagrams 3–4 & 7–10 in Fig. 2 is counterbalanced by the fact that the contributions at NLO to the M_{jjjj} spectra due to diagrams 1–2 and 5–6 in Fig 2 have no longer a symmetrical shape (compare to the same distributions at LO, especially in Fig. 6c), but this is significantly shifted towards high masses. In many cases, in fact, the phase space available for $M_{\mathrm{jjjj}} > M_H$ is much larger than that in the complementary region $M_{\mathrm{jjjj}} < M_H$. Therefore, for $\sqrt{s} \gtrsim 500$ GeV (Figs. 6b–c), the overall effect is a rather symmetrical resonance at NLO too. The same effect was not quantitatively appreciable in the case of process (1), since there the small width of the Higgs boson in the intermediate mass range drastically reduced

---

[9]Note that the appearance of a low mass 'tail' also for the LO distribution in M_{jjjj} when $M_H = 260$ GeV at $\sqrt{s} = 300$ GeV (upper dashed line in Fig. 6a, upper left plot) is accidental, as in this case the spectrum is close to its upper kinematic boundaries.

the relevance of configurations in which $M_{b\bar{b}} - M_H \gg \Gamma_H$.

The energy spectra of the emitted photon are shown in the bottom left plots of Fig. 6a–c. Again, one can see that very hard photons are not allowed if the Higgs mass/width and the CM energy are small (continuous line in Fig. 6a) and that photons created by the 'production radiation' are in most cases harder than those generated by the 'decay radiation', although the difference is less evident than for process (1). Unfortunately, this is not true at $\sqrt{s} = 300$ GeV, where the distribution of the full sample closely resembles in shape that produced by diagrams 3–4 & 7–10 in Fig. 2.

The behaviour of the spectra in p_T^{miss} (bottom right frames of Fig. 6a–c) shows that, also in the case of processes (2) and (4), the average value of the missing transverse momentum is approximately the same both at leading and at next-to-leading order. Moreover, if one studies separately the contributions to the NLO spectra due to the 'production radiation' and 'decay radiation' diagrams, one realises that once again they do not show any substantial difference, their shape being described by the lower curves in Fig. 6a–c, with appropriate normalisations.

Finally, a last comment is in order if one considers that a heavy H boson can decay into four jets also via the ZZ channel. Since BR(W → jj) ≈ BR(Z → jj) (when also b-jets are considered in the Z decay), the contribution to the total rates of the $2 \rightarrow 6$ leading order reaction $e^+e^- \rightarrow \bar{\nu}_e\nu_e H \rightarrow \bar{\nu}_e\nu_e[WW + ZZ] \rightarrow \bar{\nu}_e\nu_e$jjjj due to diagrams involving the $H \rightarrow ZZ$ decay is proportional to the corresponding branching ratio. In particular, in the heavy mass range investigated here, these are expected to be smaller by a factor of ≈ 20, for $M_H = 180$ GeV, and of ≈ 2.5, for $M_H \gtrsim 250$ GeV, compared to rates due to contributions proceeding through the $H \rightarrow WW$ channel. At next-lo-leading order, that is for the $2 \rightarrow 7$ reaction $e^+e^- \rightarrow \bar{\nu}_e\nu_e H(\gamma) \rightarrow \bar{\nu}_e\nu_e[WW + ZZ](\gamma) \rightarrow \bar{\nu}_e\nu_e$jjjj$\gamma$, a further suppression occurs. In fact, when $H \rightarrow ZZ \rightarrow$ jjjjγ, diagrams 3–4 in Fig. 2 no longer appear in the matrix element. However, the contributions of the corresponding squared amplitudes to the total cross sections of the above process are smaller than those of graphs 1–2 & 5–6, as well as than those of graphs 7–10 (Fig. 2). It varies from a few percent at small energies (i.e., $\sqrt{s} = 300$ and 500 GeV) and small Higgs masses, up to $\approx 15\%$ for $\sqrt{s} = 1000$ GeV and large values of M_H[10]. Thus, in the end, the inclusion into the calculations of diagrams involving $H \rightarrow ZZ \rightarrow$ jjjj(γ) decays could in some instances reduces the relative importance of events with hard photons. Conversely, this also indicates that experimental procedures exploiting the $H \rightarrow$ jjjj decay inclusively, or the $H \rightarrow ZZ \rightarrow$ jjjj on its own, are more likely to be less sensitive to higher order electromagnetic effects.

---

[10]We also expect an additional suppression for diagrams 7–10 of Fig. 2 when $M_H \lesssim 2M_Z$.

4. Summary and conclusions

In this paper we have studied the two radiative Higgs processes

$$e^+e^- \to \bar{\nu}_e \nu_e H(\gamma) \to \bar{\nu}_e \nu_e b\bar{b}\gamma,$$

$$e^+e^- \to \bar{\nu}_e \nu_e H(\gamma) \to \bar{\nu}_e \nu_e WW(\gamma) \to \bar{\nu}_e \nu_e \text{jjjj}\gamma.$$

We have considered the case of hard and detectable photons, by adopting the cuts $p_T^{b,\ \text{j},\gamma} > 1$ GeV, on the transverse momentum of all particles in the final states, and $\cos\theta_{b\gamma,\ \text{j}\gamma} < 0.95$, for the separation between the photon and the hadronic systems. We have then compared integrated and differential rates obtained for the two above processes to those of the reactions $(p_T^{b,\ \text{j}} > 1 \text{ GeV})$

$$e^+e^- \to \bar{\nu}_e \nu_e H \to \bar{\nu}_e \nu_e b\bar{b},$$

$$e^+e^- \to \bar{\nu}_e \nu_e H \to \bar{\nu}_e \nu_e WW \to \bar{\nu}_e \nu_e \text{jjjj}.$$

These four processes represent the main tree-level production and decay mechanisms of a Standard Model Higgs boson in the WW-fusion channel, at the centre-of-mass energies typical of an e^+e^- Next Linear Collider, at next-to-leading and leading order in the electromagnetic coupling constant, respectively. The final states $\bar{\nu}_e \nu_e b\bar{b}(\gamma)$ have been considered in order to give account of the most likely decay mechanism of the Higgs boson in the intermediate mass range $M_H \lesssim 2M_W$ (into a $b\bar{b}$ pair), whereas the $\bar{\nu}_e \nu_e \text{jjjj}(\gamma)$ ones refer to the favourite Higgs signature in the heavy mass range $M \gtrsim 2M_W$ (into four jets via WW). The values 300, 500 and 1000 GeV have been considered for $\sqrt{s}$.

Our study has been motivated by noticing that the presence of hard electromagnetic emission via bremsstrahlung photons from the initial state is somewhat unavoidable at these machines. In fact, whereas at current lower energy leptonic colliders (such as LEP1 and SLC, and partially LEP2 as well) the width of the unstable particles produced in the e^+e^- direct annihilation subprocess (Z and WW, respectively) naturally imposes a cut-off on hard photon radiation from the incoming electron and positron lines, this is no longer the case at the Next Linear Collider. Therefore one inevitably has to deal with such electromagnetic effects when attempting phenomenological analyses. Furthermore, in experimental data samples, radiative events in which the photon comes from the Higgs production mechanism are not separable from those in which it comes from the Higgs decay channels. Whereas in the former the shape of the Higgs resonances is generally not spoiled by hard photons, in the second this can in principle be heavily distorted.

Since in our computation the contributions due to the loop diagrams were missing, we have not performed a summation through the orders $\mathcal{O}(\alpha_{\text{em}}^5)$ and $\mathcal{O}(\alpha_{\text{em}}^7)$. Certainly, definite estimates of the $\mathcal{O}(\alpha_{\text{em}})$ effects should be given only after a complete calculation including

virtual photons contributions. However, the following interesting indications can be extracted from our partial results.

- Rates at next-to-leading order involving hard photons can be up to 30% of those at leading order. In particular, for all the relevant Higgs masses and CM energies considered here, these are never smaller than 10%. This corresponds to a rather large effect, in some cases comparable to or even larger than those due to beam related phenomena (such as beamsstrahlung, Linac energy spread), which are expected to take place at the high energy e^+e^- colliders of the next generation.

- The Higgs width acts as a regulator of the size of the EM emission in the Higgs decay processes. The smaller it is, the more suppressed the contribution to the total rates of diagrams involving photon radiation after Higgs production. Therefore, the smearing of the resonant distributions can be quantitatively significant only in case of Higgs masses in the heavy range (i.e., $M_H \gtrsim 2M_W$). This should remain true also for poor detector resolutions.

- If one considers heavy Higgs bosons, then two different scenarios appear.

1. For a NLC with $\sqrt{s} \gtrsim 500$ GeV, the higher order distributions relevant to Higgs searches and studies (i.e., the invariant masses of the Higgs decays products $b\bar{b}$ and jjjj) generally have a shape similar to that of the $2 \to 4$ and $2 \to 6$ leading processes. This is because the smearing of the Higgs peaks towards low masses due to the emission of hard photons in the Higgs decays is counterbalanced by a tail towards large masses due to the large portion of phase space available to photons emitted in the Higgs production mechanism. In this case, the inclusion of the complete $\mathcal{O}(\alpha_{\mathrm{em}})$ corrections is merely a matter of a different normalisation of the lowest order distributions.

2. In contrast, for a $\sqrt{s} = 300$ GeV NLC, where such phase space effects are negligible, the resonant differential spectra at NLO do show a quantitatively significant low mass tail. The effect clearly increases with the Higgs mass/width. In this case, as rates of events with hard photons can be large, a complete $\mathcal{O}(\alpha_{\mathrm{em}})$ calculation is desirable in order to assess the correct shape of the distributions at the complete NLO.

- Since events with hard and detectable photons are defined on their own once appropriate cuts are applied to remove the infrared divergences (and these can well coincide with those dictated by the tagging procedures of the experimental analyses), it is feasible to study such events separately. An interesting features of these is that the invariant masses of the systems $b\bar{b}\gamma$ (for intermediate mass Higgses) and especially jjjjγ (for heavy mass Higgses)

show a clear step/peak around the actual value of M_H. In many cases, a detectable number of events in the resonant region can be produced after a few years of running at the nominal collider luminosity.

- Distributions which could naturally allow a separation between radiative events with photons emitted in the production (on the one hand) and decay (on the other hand) stages (such as, for example, the energy of the photon and the transverse missing momentum of the neutrino pair) are not generally helpful. The p_T^{miss} spectrum presents the same behaviour for all energies and Higgs masses, both for the leading process and the two next-to-leading radiative contributions. The E_γ spectrum could be exploited in most cases, but unfortunately not when $\sqrt{s} = 300$ GeV and $M_H \gtrsim 2M_W$, since in this case the spectra of the 'production radiation' and of the 'decay radiation' are extremely similar.

In general, we stress that, in order to counterbalance the positive infrared divergences of soft and collinear (to both electron/positron and partons in the initial and final states, respectively) real EM emission, the corrections due to virtual photons in loop diagrams should generally be negative and could well reduce the relative contributions of events with the kinematics of the lowest-order processes. Therefore, the hard photon effects predicted here could well be enlarged by the complete result.

In this paper, we have also pointed out that in four-jet decays of heavy Higgs bosons proceeding through the ZZ channel (i.e., $H \to ZZ \to \text{jjjj}\gamma$) hard photon effects are smaller than in the $H \to WW(\gamma) \to \text{jjjj}\gamma$ case, but only over appropriate regions of the M_H range (that is, well above the $2M_Z$ Higgs decay threshold).

Finally, some technical details. Our computations have been performed by resorting to a numerical evaluation of the exact matrix elements of all the above processes, by means of helicity amplitude techniques, integrating them over the appropriate phase spaces, using a standard Monte Carlo routine. A dedicated treatment of the various resonant diagrams makes the `FORTRAN` code produced rather accurate and fast. In this respect, we emphasise that we have used no approximations here, apart from that of constraining the two W bosons entering in the Higgs decay channel $H \to WW(\gamma) \to \text{jjjj}(\gamma)$ to be on-shell. This has been done in order to reduce the total amount of CPU usage, especially needed when performing a $N = 3n - 5$ (assuming no transverse polarization of the beams) dimensional integration for an n-particle final state. However, the knowledge of the off-shell decay phenomenology of the Higgs boson into two W's makes straightforward the extrapolation of our results to the relevant M_H range[11]. Furthermore, some of the interferences between Feynman diagrams with

---

[11]Alternatively, the constraints on the invariant masses flowing through the W-resonances can be removed, and the integration performed over the original N dimensions, at the cost of additional CPU time.

different resonant structures have been neglected in the presentation of our results, as these are numerically negligible for the values of $\sqrt{s}$ and M_H adopted here.

Acknowledgments

References

[1] Proc. of the ECFA workshop on LEP 200, A. Bohm and W. Hoogland eds., Aachen FRG, 29 Sept.-1 Oct. 1986, CERN 87-08.

[2] Proceedings of the Workshop "*Physics and Experiments with Linear Colliders*", Saariselkä, Finland, 9-14 September 1991, eds. R. Orawa, P. Eerola and M. Nordberg, World Scientific Publishing, Singapore, 1992.

[3] Proc. of the Workshop "*e^+e^- Collisions at 500 GeV. The Physics Potential*", Munich, Annecy, Hamburg, 3-4 February 1991, ed. P.M. Zerwas, DESY pub. 92-123A/B, August 1992; DESY pub. 93-123C, December 1993.

[4] Proc. of the ECFA workshop on "*e^+e^- Linear Colliders LC92*", R. Settles ed., Garmisch Partenkirchen, 25 July-2 Aug. 1992, MPI-PhE/93-14, ECFA 93-154.

[5] Proc. of the I-IV Workshops on Japan Linear Collider (JLC), KEK 1989, 1990, 1992, 1994, KEK-Reports 90-2, 91-10, 92-1, 94-1.

[6] Proceedings of the "*Large Hadron Collider Workshop*", Aachen, 4–9 October 1990, eds. G. Jarlskog and D. Rein, Report CERN 90-10, ECFA 90-133, Geneva, 1990;
ATLAS Technical Proposal, CERN/LHC/94-43 LHCC/P2 (December 1994);
CMS Technical Proposal, CERN/LHC/94-43 LHCC/P1 (December 1994).

[7] J.D. Bjorken, Proceedings of the "*Summer Institute on Particle Physics*", *SLAC Report* 198 (1976);
B.W. Lee, C. Quigg and H.B. Thacker, *Phys. Rev.* **D16** (1977) 1519;
J. Ellis, M.K. Gaillard and D.V. Nanopoulos, *Nucl. Phys.* **B106** (1976) 292;
B.L. Ioffe and V.A. Khoze, *Sov. J. Part. Nucl.* **9** (1978) 50.

[8] D.R.T. Jones and S.T. Petkov, *Phys. Lett.* **B84** (1979) 440;
R.N. Cahn and S. Dawson, *Phys. Lett.* **B136** (1984) 196;
K. Hikasa, *Phys. Lett.* **B164** (1985) 341;
G. Altarelli, B. Mele and F. Pitolli, *Nucl. Phys.* **B287** (1987) 205;
B. Kniehl, *preprint* DESY 91-128, 1991.

[9] See for example:
A. Djouadi, D. Haidt, B.A. Kniehl, B. Mele and P.M. Zerwas, in Ref. [3], part A, and
references therein.

[10] P. Grosse-Wiesmann, D. Haidt and H.J. Schreiber, in Ref. [3], part A.

[11] T. Barklow, P. Chen and W. Kozanecki, in Ref. [3], part B, and references therein.

[12] F.A. Berends, W.L. van Neerven and G.J. Burgers, *Nucl. Phys.* **B297** (1988) 429; Erratum,
ibidem **B304** (1988) 95;
E.A. Kuraev and V.S. Fadin, *Sov. J. Nucl. Phys.* **41** (1985) 466;
G. Altarelli and G. Martinelli, Proceedings of the Workshop '*Physics at LEP*', eds. J. Ellis
and R. Peccei, Geneva, 1986, CERN 86-02;
R. Kleiss, *Nucl. Phys.* **B347** (1990) 29;
O. Nicrosini and L. Trentadue, *Phys. Lett.* **B196** (1987) 551; *Z. Phys.* **C39** (1988) 479.

[13] V. Barger, K. Cheung, A. Djouadi, B.A. Kniehl, R.J.N. Phillips and P.M. Zerwas, in
Ref. [3], part C.

[14] K. Hagiwara and D. Zeppenfeld, *Nucl. Phys.* **B274** (1986) 1.

[15] H. Murayama, I. Watanabe and K. Hagiwara, HELAS: HELicity Amplitude Subroutines
for Feynman Diagram Evaluations, *KEK Report* 91-11, January 1992.

[16] T. Stelzer and W.F. Long, *Comp. Phys. Comm.* **81** (1994) 357.

[17] G.P. Lepage, *Jour. Comp. Phys.* **27** (1978) 192.

[18] S. Moretti, *preprint* DFTT 78/95, Cavendish–HEP–95/17, revised February 1996 (to appear in *J. Phys.* **G**), and references therein.

[19] E. Braaten and J.P. Leveille, *Phys. Rev.* **D22** (1980) 715;
N. Sakai, *Phys. Rev.* **D22** (1980) 2220;
T. Inami and T. Kubota, *Nucl. Phys.* **B179** (1981) 171;
M. Drees and K. Hikasa, *Phys. Lett.* **B240** (1990) 455;
S.G. Gorishny, A.L. Kataev, S.A. Larin and L.R. Surguladze, *Mod. Phys. Lett.* **A5** (1990)

2703;

L.R. Surguladze, *Phys. Lett.* **B341** (1994) 60.

[20] D. Bardin, M. Bilenky, A. Olchevski and T. Riemann, *Phys. Lett* **B308** (1993) 403; Erratum, *ibidem* **B357** (1995) 725.

[21] D. Bardin, D. Lehner and T. Riemann, *preprint* DESY 96-028, February 1996.

[22] T. Kinoshita, *J. Math. Phys.* **3** (1962) 650;
T.D. Lee and M. Nauenberg, *Phys. Rev.* **133B** (1964) 1549.

[23] V.V. Sudakov, *Sov. Phys. JETP* **3** (1956) 65.

Figure Captions

Fig. 1 Feynman diagrams contributing at tree-level to process (1).

Fig. 2 Feynman diagrams contributing at tree-level to process (2).

Fig. 3 Cross sections of the processes (1) and (3) as a function of the Higgs mass, at $\sqrt{s} = 300$ GeV (upper plot), $\sqrt{s} = 500$ GeV (central plot), $\sqrt{s} = 1000$ GeV (lower plot), after the cuts $p_T^{b,\gamma} > 1$ GeV and $\cos\theta_{b\gamma} < 0.95$.

Fig. 4 Cross sections of the processes (2) and (4) as a function of the Higgs mass, at $\sqrt{s} = 300$ GeV (upper plot), $\sqrt{s} = 500$ GeV (central plot), $\sqrt{s} = 1000$ GeV (lower plot), after the cuts $p_T^{j,\gamma} > 1$ GeV and $\cos\theta_{j\gamma} < 0.95$.

Fig. 5 Distributions in invariant mass of the $b\bar{b}$ pair (upper left plot), in invariant mass of the $b\bar{b}\gamma$ system (upper right plot), in energy of the photon (lower left plot) and in missing transverse momentum (lower right plot) for processes (1) and (3), after the cuts $p_T^{b,\gamma} > 1$ GeV and $\cos\theta_{b\gamma} < 0.95$, for a selection of Higgs masses: (**a**) at $\sqrt{s} = 300$ GeV (bins of 2 GeV); (**b**) at $\sqrt{s} = 500$ GeV (bins of 4 GeV); (**c**) at $\sqrt{s} = 1000$ GeV (bins of 5 GeV). In the first and third plot (clockwise) the upper histograms refer to rates from the non-radiative process (3), whereas the lower histograms correspond to rates from the radiative process (1). In the first plot the lowest order rates are shaded. In the fourth plot the upper histograms refer to rates from the complete set of diagrams describing process (1), whereas the lower histograms correspond to rates from contributions due to 'decay radiation' graphs only.

**Fig. 6** Distributions in invariant mass of the 4jet system (upper left plot), in invariant mass of the 4jetγ system (upper right plot), in energy of the photon (lower left plot) and in

missing transverse momentum (lower right plot) for processes (2) and (4), after the cuts $p_T^{j,\gamma} > 1$ GeV and $\cos\theta_{j\gamma} < 0.95$, for various selections of Higgs masses: (**a**) at $\sqrt{s} = 300$ GeV (bins of 2 GeV); (**b**) at $\sqrt{s} = 500$ GeV (bins of 4 GeV); (**c**) at $\sqrt{s} = 1000$ GeV (bins of 5 GeV). In the first and third plot (clockwise) the upper histograms refer to rates from the non-radiative process (4), whereas the lower histograms correspond to rates from the radiative process (2). In the first plot the lowest order rates are shaded. In the fourth plot the upper histograms refer to rates from the complete set of diagrams describing process (2), whereas the lower histograms correspond to rates from contributions due to 'decay radiation' graphs only.
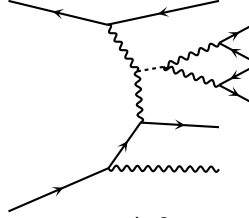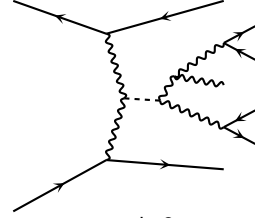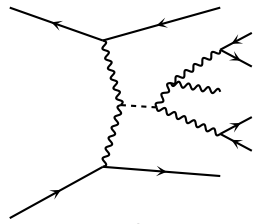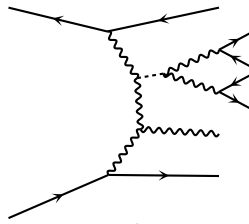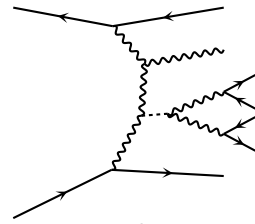
Diagrams by MadGraph

graph 1

graph 2

graph 3

graph 4
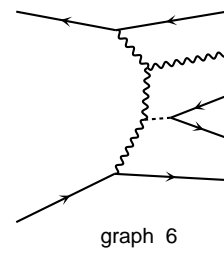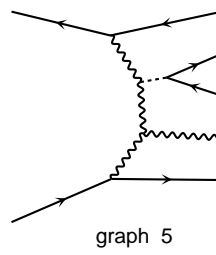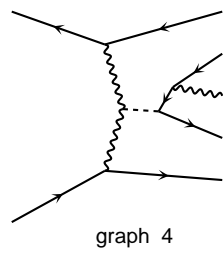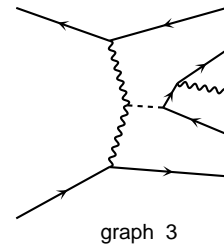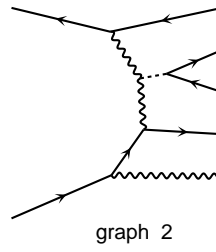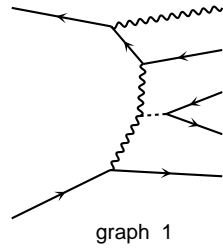
graph 5

graph 6

Fig. 1
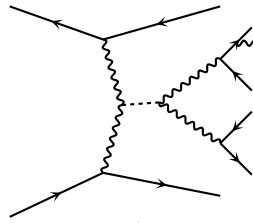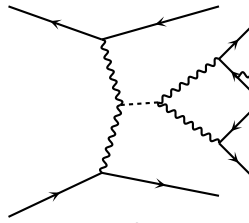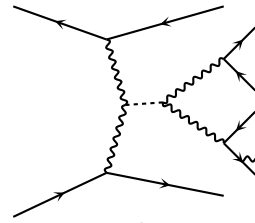
Diagrams by MadGraph
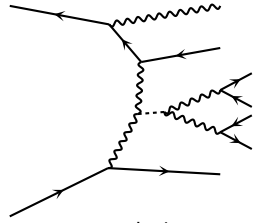
graph 1

graph 2

graph 3

graph 4

graph 5

graph 6

graph 7

graph 8

graph 9

graph 10

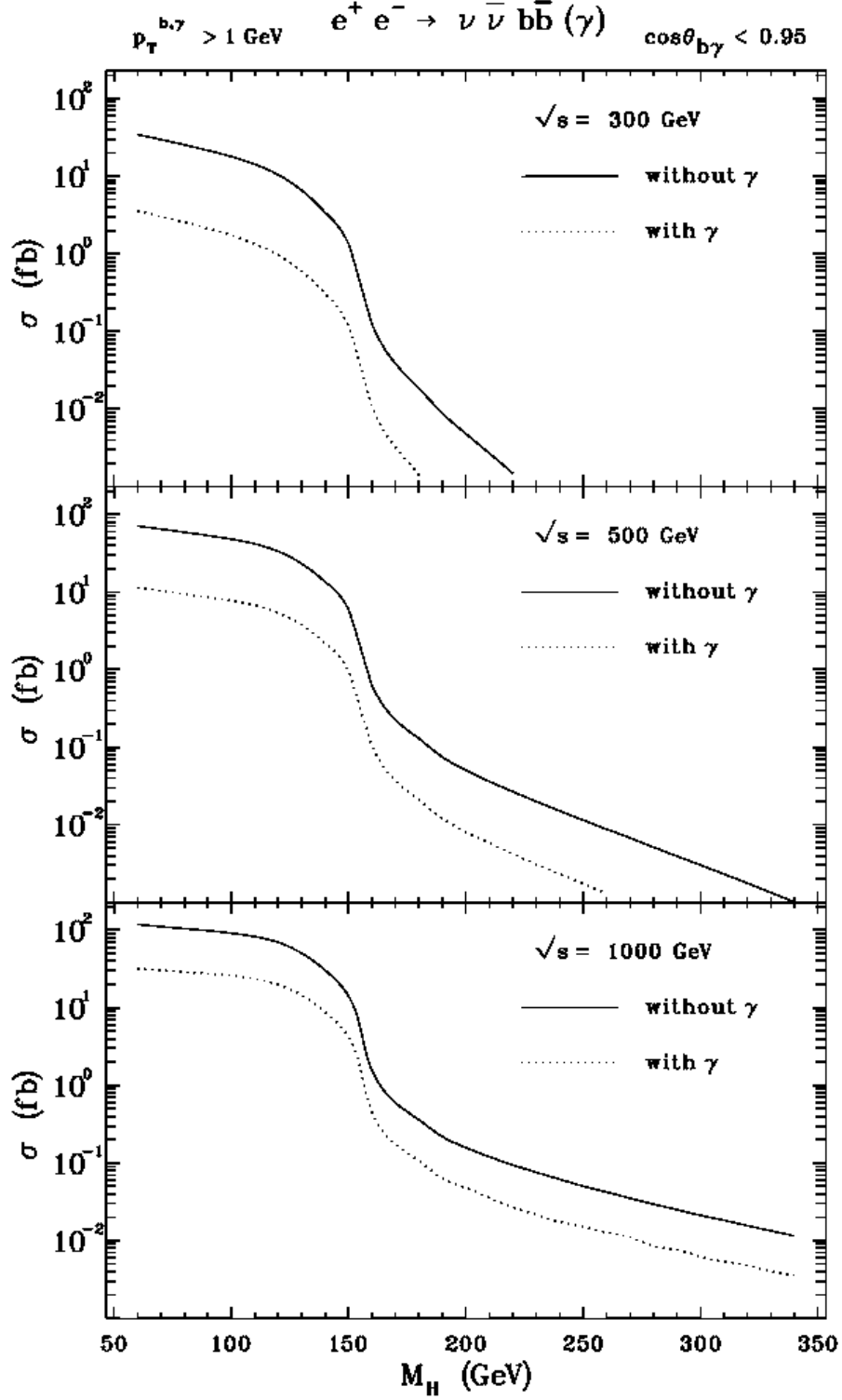Fig. 2

19

$p_T^{b,\gamma} > 1$ GeV $\qquad e^+ e^- \to \nu \bar{\nu} b\bar{b} (\gamma) \qquad \cos\theta_{b\gamma} < 0.95$

$\sqrt{s} = 300$ GeV

without γ

with γ

$\sqrt{s} = 500$ GeV

without γ

with γ

$\sqrt{s} = 1000$ GeV

without γ

with γ

M_H (GeV)

Fig. 3

20

$p_T^{j,\gamma} > 1$ GeV $\qquad e^+ e^- \to \nu \bar{\nu} \, jjjj \, (\gamma) \qquad \cos\theta_{j\gamma} < 0.95$

$\sqrt{s} = 300$ GeV

without γ

with γ

$\sqrt{s} = 500$ GeV

without γ

with γ

$\sqrt{s} = 1000$ GeV

without γ

with γ

M_H (GeV)

Fig. 4

$e^+ e^- \rightarrow \nu \bar{\nu} b\bar{b} (\gamma)$

$p_T^{b,\gamma} > 1$ GeV $\sqrt{s} = 300$ GeV $\cos\theta_{b\gamma} < 0.95$

$M_H = 60$ GeV $M_H = 100$ GeV $M_H = 140$ GeV

Fig. 5a

22

$e^+ e^- \rightarrow \nu \bar{\nu} b\bar{b} (\gamma)$

$p_T^{b,\gamma} > 1$ GeV $\qquad \sqrt{s} = 500$ GeV $\qquad \cos\theta_{b\gamma} < 0.95$

$M_H = 60$ GeV $\qquad M_H = 100$ GeV $\qquad M_H = 140$ GeV

Fig. 5b

23

$e^+ e^- \rightarrow \nu \, \bar{\nu} \, b\bar{b} \, (\gamma)$

$p_T^{b,\gamma} > 1$ GeV $\sqrt{s} = 1000$ GeV $\cos\theta_{b\gamma} < 0.95$

$M_H = 60$ GeV $M_H = 100$ GeV $M_H = 140$ GeV

Fig. 5c

24

$$e^+ e^- \rightarrow \nu \bar{\nu} \, jjjj \, (\gamma)$$

$p_T^{j,\gamma} > 1$ GeV $\sqrt{s} = 300$ GeV $\cos\theta_{j\gamma} < 0.95$

$M_H = 180$ GeV $M_H = 220$ GeV $M_H = 260$ GeV

Fig. 6a

25

$$e^+ e^- \rightarrow \nu \bar{\nu} jjjj (\gamma)$$

$p_T^{j,\gamma} > 1 \text{ GeV}$ $\sqrt{s} = 500 \text{ GeV}$ $\cos\theta_{j\gamma} < 0.95$

——— $M_H = 180 \text{ GeV}$ ·········· $M_H = 260 \text{ GeV}$ — — — $M_H = 340 \text{ GeV}$

Fig. 6b

$$e^+ e^- \to \nu \bar{\nu} \, jjjj \, (\gamma)$$

Fig. 6c